APS/123-QED

Frequency domain characterization of tuning-fork mechanical vibrations by vision and digital image processing

P. Sandoz*

FEMTO-ST/LOPMD, 16 route de Gray,

UFR-ST La Bouloie, 25000 Besançon, FRANCE

J.-M. Friedt

Association Projet Aurore, UFR-ST La Bouloie,

16 route de Gray, Besançon, FRANCE

É. Carry

FEMTO-ST/LOPMD, 16 route de Gray,

UFR-ST La Bouloie, 25000 Besançon, FRANCE

B.Trolard

Association Projet Aurore, UFR-ST La Bouloie,

16 route de Gray, Besançon, FRANCE

J. Garzon Reyes

Grupo de Óptica y Espectroscopía, Centro de Ciencia Básica,

Universidad Pontificia Bolivariana. Cq. 1 No. 70-01, Medellín, Colombia

(Dated: February 12, 2008)

Abstract

We demonstrate an experimental setup and the associated digital image processing software for measuring the vibration amplitude of a tuning fork with sub-pixel accuracy. Stroboscopic illumination allows the use of a standard video rate camera for the exploration of resonant frequencies up to the kHz range. No preliminary surface patterning is required since the image processing is based on the natural features present in the object structure. The amplitude response of the tuning fork is explored in the frequency domain and the resonance is characterized. We use the property of the tuning fork of being a high quality-factor resonator for demonstrating the spectral power distribution of various excitation signals as well as the temperature dependance of the resonance frequency. The results presented here can be generalized to the measurement of 2D in-plane lateral displacements of any structure.

PACS numbers: 07.79.-v

Keywords: tuning fork, digital image processing, vibration amplitude

I. INTRODUCTION

Measuring the displacement of vibrating mechanical structures is a recurring problem for characterizing the material properties or the eigenmodes of an object. Out-of-plane displacements are usually characterized with holographic or interferometric methods leading to subwavelength accuracies. In-plane displacement characterization presents a challenge which can be mostly addressed by digital image processing methods. Crude methods such as sampling with a period much shorter than the vibration under investigation provide results limited by either the pixel size or the contrast of the available structures on the object[1]. Measuring the vibration amplitude of oscillating resonators with sub-pixel accuracy requires a stroboscopic illumination coupled with efficient image processing methods[2]. In this paper, we wish to apply such a technique to the characterization of an acoustic tuning fork. We chose this kind of device since tuning forks are widely used in undergraduate teaching for illustrating resonator characteristics. However, beyond microphone recording of the sound generated by the tuning fork upon being hit by a hard object[3], little is known of the actual characteristics of the tuning fork itself such as its quality factor or the temperature dependence of the resonance frequency. Such measurements require means to measure the mechanical vibration of the tuning fork subject to a continuous excitation. In this paper, we demonstrate this kind of experimental analysis with emphasis on the following purposes:

- characterize the fundamental properties of the vibrating object under investigation: identification of its eigenmode frequency, vibration amplitude, quality factor ...,
- demonstrate how commonly available equipment (personal computer with a sound card, audio amplifier and a USB camera) can be used for precise measurements of a vibrating structure thanks to digital image processing,
- illustrate some of the well-known Fourier energy distribution characteristics of classical waveforms (sine, triangle, square) on a physical system, and the dependency of the properties of this physical system on its environment (temperature).

II. EXPERIMENTAL METHODS

We aim at visualizing the tuning fork vibration in a continuous, forced regime, and at measuring it accurately while the excitation frequency is swept. Then the tuning fork can be fully characterized in the frequency domain. Our wish is also to make the setup affordable for teaching. Therefore, the tuning fork motion has to be observed at standard video rate with a commonly used camera[4]. We chose a CMOS camera (uEye UI-1540-M) connected to the USB port of the personal computer and a C-mount zoom lens (Computar MLH-10x) to form the image of the prong-end surface on the image sensor. The observation of vibrations up to the kHz range at video-rate assumes a stroboscopic illumination with a phase control with respect to the tuning fork excitation. We choose to generate the drive signals by means of the stereo sound card of a personal computer. One channel is used for tuning fork excitation while the second one produces the pulses for driving the LED (Luxeon Star/LXHL MWEA) used as light source. These control signals are synthesized by custom software with a frequency resolution of 0.1 Hz, limited only by the length of the buffer in which the signal is computed. One advantage of software synthesis of the signals, beyond requiring little hardware and hence being cost-effective, is the ease with which various signal shapes can be selected. Only few commercial synthesizers provide synchronized outputs based on the same reference clock, these instruments being usually unavailable for teaching. We have successfully used the Tektronix AFG320 for replacement of the sound card output.

We also had to identify a suitable excitation method for transferring energy from an actuator to the tuning fork. We have used a speaker located close to the end of one prong to put the tuning fork in motion without mechanical contact[5–9]. Energy transfer results from a combination between magnetic and acoustic coupling as discussed later. The speaker position is adjusted with respect to one prong of the tuning fork using a positioning table with a sub-millimeter accuracy for best results. We will discuss later (section IV) the stability of the vibration amplitude resulting from this excitation method.

[FIG. 1 about here.]

(Fig. 1) presents the schematic as well as a picture of the experimental setup. A further two-channel audio amplifier (Sony XM-SD12X 250 W) can be recognized that amplifies the sound card outputs to the levels required for driving both the LED and the speaker. A 2Hz frequency shift is systematically applied between speaker excitation and LED triggering. This choice produces a linear phase shift between tuning fork excitation and illumination. Therefore the prong motion is observed with an apparent frequency of 2Hz; compatible with the standard video rate. The LED is triggered by pulses 60 μs-long ensuring negligible averaging of the prong motion. Thus video sequences of the prong motion are recorded and the vibration amplitude is retrieved by digital processing of these image sequences as explained in sect.III.

[FIG. 2 about here.]

Fig.2 presents recorded images of the end face of one prong of the tuning fork with different magnifications adjusted by means of the zoom lens. Magnification is determined by imaging calibrated patterns and the vibration measurements reported here were performed with an actual pixel size of $5.8\mu m$ on the object.

III. IMAGE PROCESSING METHODS

Under the experimental conditions described above, the tuning fork oscillations induce a rigid-body lateral displacement of the prong end face under observation. The aim of image processing is then to retrieve the lateral displacement values from the image sequences recorded. Various methods can be thought for this purpose. The most conventional would be to use image cross-correlation. Then, the location of the correlation peak gives directly the displacement value. Subpixel accuracy can be obtained by over-sampling digitally the initial images. Other techniques were also reported for improving the correlation resolution[11–13].

Instead of using the well-known correlation method, we choose a different approach based on an interesting property of the phase of the Fourier transform. In this section, we first present the pure phase shift produced in the Fourier spectrum by a lateral shift of the object in the spatial domain. Then, we introduce the working principle of an iterative algorithm retrieving the spatial displacement by processing the spectral phase. Finally we discuss results obtained with this approach as well as side effect considerations.

One may notice the following points with respect to this technical issue of image processing:

- Firstly, the phase approach used is an opportunity to emphasize on the useful relationship between spectral phase and relative displacement in the spatial (or temporal) domain. The latter is widely unknown since Fourier transform is primarily known as an efficient tool for spectral component extraction or rejection through suitable filtering of the Fourier spectrum and inverse Fourier transform.
- Secondly, Matlab code sources can be downloaded for immediate implementation of the required image processing[14]. Experimental images are also available for demonstration.
- Thirdly, the iterative algorithm can be avoided by using image cross-correlation that provides subpixel resolution also.

A. Relationship between spatial displacement and spectral phase

Let us consider the lateral displacement of the prong end face under observation as a rigid-body motion. Then the image recorded at time t_i is a shifted form of the image recorded at time $t = 0$ and can be expressed as :

$$I_i(x, y) = I_0(x, y) * \delta(\Delta_x, \Delta_y) \tag{1}$$

where $*$ stands for the convolution product, δ stands for the Dirac impulse distribution and (Δ_x, Δ_y) is the lateral shift between the two images. This expression does not consider the finite extension of the imaged area that makes that the objects observed before and after displacement are not rigorously identical. This point and consecutive "side effects" will be discussed later but let us first accept Eq.1. With this assumption, let us consider the Fourier transform of Eq.1:

$$\widetilde{I}_i(u, v) = \widetilde{I}_0(u, v) \cdot exp(2\pi u\Delta_x) \cdot exp(2\pi v\Delta_y) \tag{2}$$

where u, v are the spatial frequencies reciprocal of x, y and $\widetilde{I}(u, v)$ stands for the Fourier transform of $I(x, y)$. This expression shows clearly that the effect of a lateral displacement in the space domain only modifies the phase in the spectral domain[10]. Then the phase difference $\Delta\phi(u, v)$ between the Fourier spectra before and after displacement can be written:

$$\Delta\phi(u, v) = 2\pi u\Delta_x + 2\pi v\Delta_y \tag{3}$$

This phase difference is a tilted plane whose slopes versus u and v are directly proportional to the displacement involved. Therefore, the identification of the displacement is obvious from the knowledge of the map of the spectral phase difference.

The application of these principles to actual image processing is more complicated because of the way of determining the spectral phase. The argument of the complex spectrum results from an inverse tangent function that is defined only in the interval $[-\pi, \pi)$. Thus the wrapped phase difference available numerically has the form:

$$\delta\phi(u_i, v_j) = \Delta\phi(u_i, v_j) + 2\pi k_{ij} \tag{4}$$

where (i, j) are the indexes of the digital image and k_{ij} is an integer resulting from the 2π modulus operation at pixel (i, j). Thus the actual starting point of the digital processing dedicated to the retrieval of the displacement (Δ_x, Δ_y) is given by Eq.4 that is less convenient than Eq.3 because of k_{ij} constants. The k_{ij} constants have to be identified before to determine the object displacement from Eq.3. This problem is a particular case of phase unwrapping since we know *a priori* that the final result is a phase plane. We applied a known iterative algorithm as described below.

B. Iterative algorithm for displacement retrieval

We used a solution based on a spectral phase algorithm. The latter has been proposed and applied to the identification of the center of a symmetrical object in 1D[15] and then in 2D[16]. It is well known that the Fourier spectrum of a symmetrical object (or even function) is real. Therefore the spectral phase map is uniformly equal to zero. If such an object is shifted from the central position, the spectral phase of the corresponding Fourier spectrum is directly given by the exponential terms of Eq.2. Therefore the phase difference of Eq.4 is directly given by the wrapped phase of a single Fourier spectrum. Then, the algorithm proposed by Oriat[16] can be applied to object displacement measurements; as it was already demonstrated on speckle pattern images[17]. Details can be found elsewhere[15,16] and we just present here the basic principle of the algorithm. The starting assumption is that the image displacement remains smaller than $(M/a, N/b)$ where M and N are image size in pixels and a and b are constants typically equal to 8 or 16. This condition implies that the k_{ij} constants are equal to zero for spatial frequencies smaller than $(M/2a, N/2b)$. Thus, a first estimate of the displacement is evaluated from this restricted set of spatial frequencies. Then this coarse value is used for the prediction of the k_{ij} constants of the neighboring spatial frequencies and a new estimate of the displacement based on a larger set of spatial frequencies. This prediction - correction procedure is repeated by considering one additional spatial frequency at each iteration. Thus, the displacement estimate converges progressively toward the actual one. This principle is implemented with a specific monitoring of noise. The phase of a Fourier spectrum is known to be very sensitive to noise; especially for low-modulus spectral components. In the recursive algorithm used, the phase values are weighed by their modulus in order to give the largest importance to the spatial frequencies that are the most representative of the object. The image processing software used as well as demonstration images are available on line[14].

C. Reconstructed displacements and discussion

Fig.3 presents a typical case of algorithm convergence toward the actual displacement values.

[FIG. 3 about here.]

For the processing of video sequences recorded as explained before, the displacement of each image is computed with respect to the first image that is taken as a reference. Fig.4 presents a typical result of prong displacement measurement as reconstructed with the spectral phase algorithm.

[FIG. 4 about here.]

Discontinuities can be observed in the displacement curve. This results from missing images in the video sequences and appears because of excessive computer load. This can be avoided by managing properly the central processing unit activity. A practical solution is to record twice the same sequence, since cache memory has been allocated during the first execution of the software and is still available for immediate access during the second run: the second one overwrites the memory space used for the first one and in our case no images are missing.

The accuracy of the spectral phase method was validated by using another method[18]. For that purpose a dot pattern printed on a small piece of paper was stuck on the prong end and results obtained with the two methods were compared successfully.

The spectral phase algorithm was also compared with image cross-correlation[17]. The spectral phase algorithm was found to be a little bit faster than image cross-correlation with peak interpolation methods while achieving the same accuracy in displacement measurements.

The spectral phase algorithm used assumes that the object images can be considered to be the same before and after displacement. The analytical definition of the acceptance limits of this assumption would be very difficult to define. Experimentally, the algorithm was found to be very robust for object displacements up to 8 to 15 pixels and for computations based on an region of interest (ROI) of 128×128 pixels. Therefore excellent results were obtained as presented in the following. However, the object dependence of the algorithm robustness can be easily demonstrated experimentally. If the ROI is selected in such a way that one or several bright spots are close to the frontier, object motions make it that these spots are alternatively visible or not, at least partially. Then we can observed that the maximum vibration amplitude acceptable for algorithm convergence is reduced (down to 5 pixels or less). This observation emphasizes the weight of these high-energy object features on the image spectrum, even for low spatial frequencies. On the opposite, if the ROI is shifted in order to concentrate the main part of the object energy in the central part, then much larger displacements are acceptable (more than 20 pixels) by keeping the same vibration amplitude. Discrete Fourier transform algorithms are also involved in the manifestation of this phenomenon. This kind of experimental observations is of particular interest in teaching environment. This problem is analogous to the problem of object likeliness in the case of image cross-correlation. One may also notice that both methods do not work in case of image rotation.

IV. RESULTS

As described further in the text, the setup and the image processing software allow a complete exploration of the tuning fork's behavior, a characterization of the tuning-fork excitation used as well as the didactic observation of known properties of signal theory.

A. Tuning fork excitation and resonance curve

The description of the resonance curve of the tuning-fork is the result expected primarily from a frequency domain analysis. This study was carried out by measuring the prong vibration amplitude versus the frequency of the sine wave applied to the speaker. Fig.5 plots the curve obtained. The resonance frequency is close to 439.9Hz and the quality factor was estimated to be equal to $Q = 2500 \pm 200$.

[FIG. 5 about here.]

Let us now investigate the physical phenomenon involved in the non contact energy transfer from the speaker to the tuning fork. This analysis was carried out by increasing progressively the distance separating the speaker from the prong. Whatever the excitation frequency, the tuning fork vibration amplitude was found to be dependent of this distance as represented in Fig.6. The efficiency of the energy transfer is highest when the prong is closest to the speaker. As the distance is increased, the energy transfer efficiency decreases rapidly, experiments a minimum and then increases up to a medium efficiency that is slowly decreasing as a function of the distance. We interpret this curve as the combination of magnetic and acoustic coupling. At very short distances, the dominant effect is due to the modulation of the magnetic attraction exerted on the ferromagnetic material of the prong. This modulation results from the alternative current flowing through the coil. The discrepancy of this magnetic force follows a $1/r^3$ law versus the distance. Then, this effect vanishes rapidly as the distance is increased. The second phenomenon is the acoustic coupling. Because of the speaker (55 mm in diameter), tuning fork (80 mm for the prong length) and acoustic wavelength (0.775 m at 440 Hz) sizes, no significant variation of the acoustic coupling can be expected with a variation of the speaker-prong distance of a few millimeters[19]. The efficiency of the acoustic coupling varies necessarily slowly in the centimeter range of distances considered here. The minimum observed in the curve is due to superposition of the two phenomena with opposite phases.

The acoustic and magnetic forces produced by the speaker can be either in or out of phase depending on the disposal of the different parts. The actual direction of the coil displacement is determined by the orientations of both the permanent magnetic field and the current flowing through the coil. On the opposite, the alternative magnetic field produced by the coil is only determined by the orientation of the current flowing through it. Therefore, by simply reversing the magnet poles, the direction of the coil motion can be changed without modifying the alternative magnetic field. Then the motions of the coil and of the alternative magnetic field can be either oriented in the same direction or in opposite directions. Fig.7 presents the two possibilities by simply changing the relative position of the coil and of the membrane with respect to the magnet.

These consideration are not of interest for the intrinsic - i.e. acoustic - specifications of a speaker. Then we probably have a random distribution of in phase or out of phase cases among a series of different speakers. This could be verified experimentally in a teaching environnement.

[FIG. 6 about here.]

[FIG. 7 about here.]

B. Experimental observation of known physical effects

Because of its high quality factor the tuning fork is a very selective frequency filter. Its vibration amplitude is a reliable indicator of the presence of its resonance frequency band in the spectrum of the excitation signal. We have used this faculty for the didactic demonstration of well known signal theory properties. Fig.8 presents two examples of vibration amplitudes as measured when the excitation is turned on. We can observe that the vibration amplitude does not increase monotonously but undergoes oscillations that are more intense than the final forced regime. This observation illustrates the broadening of the Fourier spectrum of sine signals because of their short duration[20]. Indeed, the spectrum of a sine wave at angular frequency $\omega = 2\pi \times f$ generated during a time T is $\frac{\sin(\omega T)}{\omega T}$, *i.e.* a broadband signal for short T. In our case this broadband excitation means that the sharp initialization of the sound card induces the vibration of the tuning fork on its resonance frequency f_r, while further excitation at $f \neq f_r$ induces a beat with period $|f - f_r|^{-1}$. The amplitude modulation observed here hence provides the difference between the forced regime frequency f and the resonance frequency f_r. The beat signal will remain for a duration of order Q/π periods with Q the quality factor of the tuning fork (notice that Q/π periods is also the duration the sound generated by the tuning fork can be heard after being hit on a hard surface: it is typically a few seconds).

Having waited long enough for the forced regime to establish (*i.e.* for the natural resonance frequency component to die out), we indeed observe that the vibration amplitude is constant with constant excitation voltage sent to the speaker. Such graphics are of great interest since they provide an accurate means of identifying the resonance frequency of the tuning fork.

[FIG. 8 about here.]

These examples illustrate that a gated sine wave induces a broadband signal, the shorter the duration of the excitation, the broader the range of frequencies generated. The two asymptotic cases are obviously the pulse which generates all frequencies within the frequency range of the amplifier, and the continuous frequency generation which induces a forced regime at a fixed frequency. Other common cases are the triangle and square shaped excitation signals which are easily synthesized by the sound card and for which the energy distribution in the overtone frequencies is well known: $1/(2N+1)^2$ and $1/(2N+1)$ respectively for overtone (2N+1) of the excitation frequency. We observed experimentally these signal theory properties by sending various signal shapes to the speaker at frequency $f_r/3$.

[FIG. 9 about here.]

Results presented in Fig.9 demonstrate clearly that the tuning-fork can be excited at its resonant frequency by a non-sinusoidal excitation signal at $f_r/3$. The vibration amplitude was found to be 4.25 times larger for the square signal than for the triangle signal while the sine signal does not induce vibrations. One may expect a ratio of 3 instead of 4.25. In fact the power of the overtones of a triangle signal with respect to a square signal depends on the mean power carried by each signal. In our case, we worked at constant amplitude and the square signal supplies more power than the triangle one.

We evaluated these measurements of the tuning fork amplitude through a spectrum analysis of the excitation signals by means of a HP3582A spectrum analyser. Results obtained are summarized in Tab.I. The case of the sine signal is obvious since there are no harmonics. Square and triangle signals present overtones as expected and their relative power with respect to the fundamental component is in agreement with the theoretical law of $1/(2N+1)$ and $1/(2N+1)^2$ respectively. Furthermore, the ratio of 4.4 between square and triangle shapes at the tuning fork resonant frequency is consistent with the 4.25 factor resulting from Fig.9.

[TABLE 1 about here.]

In order to assess the resonance frequency drift with temperature, we have performed several resonance frequency measurements at various temperatures (Fig. 10). We observe a resonance frequency shift of 0.057 Hz/3.5^{o}C following the fit of the experimental data with a damped oscillator model for improving the accuracy of the resonance frequency identification.

We know[21] that the resonance frequency f of a tuning fork is related to $f \propto \frac{a}{l^2}\sqrt{\frac{E}{\rho}}$ where a is the thickness of the tuning fork, l its length, E and ρ being respectively the Young modulus and the density of the material the tuning fork is made of. Most metals display a dilatation temperature coefficient around $s = 2 \times 10^{-5}$ so that the contribution of the dimension of the prongs to the frequency shift is $\Delta f/f = -\Delta l/l = s$ *i.e.* $\Delta f = f \times s \simeq$ 0.01 Hz/K, assuming E and ρ independent of temperature. This result is in accordance with the measured value of 0.016 Hz/^{o}C considering the uncertainty on the dilatation coefficient and the prong temperature which was measured with a Pt100 probe located in an air-conditioned room.

[FIG. 10 about here.]

V. CONCLUSION

We have demonstrated a digital image processing setup and method for characterizing in-plane 2D-vibration amplitudes in the audio frequency range with sub-pixel accuracy. We have applied these techniques to the characterization of a tuning fork. The method uses surface defects for motion detection and hence requires no additional patterning of the sample being observed.

We have used the result of signal processing for the illustration of classical quantities characterizing a high quality factor resonator as provided here by the tuning fork: quality factor, forced regime stabilization time, energy distribution in overtones of usual signal shapes, and temperature dependence of the resonance frequency.

We have taken care to use as little hardware as possible to keep the experimental setup compatible with a teaching budget: the stroboscopic illumination signal synchronized with the acoustic excitation signal are both generated by the two stereo channels of a computer sound card, while images are recorded from a camera connected to a USB port of this same computer. The software used in this presentation (sound generation and signal processing algorithm implementations under Matlab) are available on-line[14].

VI. ACKNOWLEDGEMENT

---

* Electronic address: `patrick.sandoz@univ-fcomte.fr`

1 B. Borovsky, B. L. Mason, and J. Krim, "Scanning tunneling microscope measurements of the amplitude of vibration of a quartz crystal oscillator", J. Appl. Phys., **88**, 4017-4021, (2000).

2 X. Chen, J. Huang, and E. Loh, "Two-dimensional fast Fourier transform and pattern processing with IBM PC", Am. J. Phys, **56**, 747-749, (1988).

3 M.J. Moloney, "Simple acoustic source radiation near a large wall", Am. J. Phys, **71**, 794-796, (2003).

4 J.R. Wang, I.C. Huang, T.C. Fang, F.Y. Yang, S.F. Tsai, Y.I. Chang, and P.K. Tseng, "An application of video-camera and PC-oriented image processor to an experiment on the coherent property of light", Am. J. Phys, **58**, 405-407, (1990).

5 R.B. Dow, "The Electrically Driven Tuning Fork as a Source of Constant Frequency for the Precise Measurement of Short Intervals of Time", Am. J. Phys, **4**, 199-200, (1936).

6 G.A. Doran, "Electronically Maintained Tuning Fork for Use by Students", Am. J. Phys, **28**, 505-506, (1960).

7 W. L. Lama, R. Jodoin, and L. Mandel, "Superradiance in Radiatively Coupled Tuning Forks", Am. J. Phys, **40**, 32-37, (1972).

8 T. H. Ragsdale and W. L. Davis, "Tuning out the tuning forks", Am. J. Phys, **50**, 1170-1171, (1982).

9 D.A. Russell, "On the sound field radiated by a tuning fork", Am. J. Phys, **68**, 1139-1145, (2000).

10 I. Juvells, S. Vallmitjana, A. Carnicer, and J. Campos , "The role of amplitude and phase of the Fourier transform in the digital image processing", Am. J. Phys, **59**, 744-748, (1991).

11 J. Riera, J.A. Monsoriu, M.H. Gimé nez, J.L. Hueso, and J.R. Torregrosa, "Using image recog-

nition to automate video analysis of physical processes", Am. J. Phys, **71**, 1075-1079, (2003).

[12] M. Sjödahl, L.R. Benckert, "Electronic speckle photography: analysis of an algorithm giving the displacement with subpixel accuracy", Appl. Opt., **32**, 2278-2284, (1993).

[13] J. Zhang, G. Jin, S. Ma, L. Meng, "Application of an improved subpixel registration algorithm on digital speckle correlation measurement", Opt. and Laser Tech., **35**, 533-542, (2003).

[14] `http://jmfriedt.free.fr`

[15] E. Lantz, "Subpixel signal centering and shift measurement using a recursive spectral phase algorithm", Signal Processing, **17**, 365-372, (1989).

[16] L. Oriat, E. Lantz, "Subpixel detection of the center of an object using a spectral phase algorithm on the image", Pattern Recognition, **31**, 761-771, (1998).

[17] C. Poilâne, "Caractérisation mécanique des matériaux en faible épaisseur par interférométrie numérique. Application aux essais de gonflement et de traction", PhD dissertation, Université de Franche-Comté, France, (1998).

[18] P. Sandoz, J.-M Friedt, and É. Carry, "In-plane rigid-body vibration mode characterization with a nanometer resolution by stroboscopic imaging of a microstructured pattern", Review of Scientific Instruments **78**, 023706 (2007).

[19] R. M. Sillitto, "Angular Distribution of the Acoustic Radiation from a Tuning Fork", Am. J. Phys, **34**, 639-644, (1966).

[20] A.L. Boreen, R.L. Coons, D.J. Ulness, B.A. Luther, "Investigating collisional broadening of spectral lines using a tuning fork: An undergraduate laboratory", Am. J. Phys, **68**, 768-771, (2000).

[21] T.D. Rossing, D.A. Russell, and D.E. Brown, "On the acoustics of tuning forks", Am. J. Phys, **60**, 620-626, (1992).

List of Figures

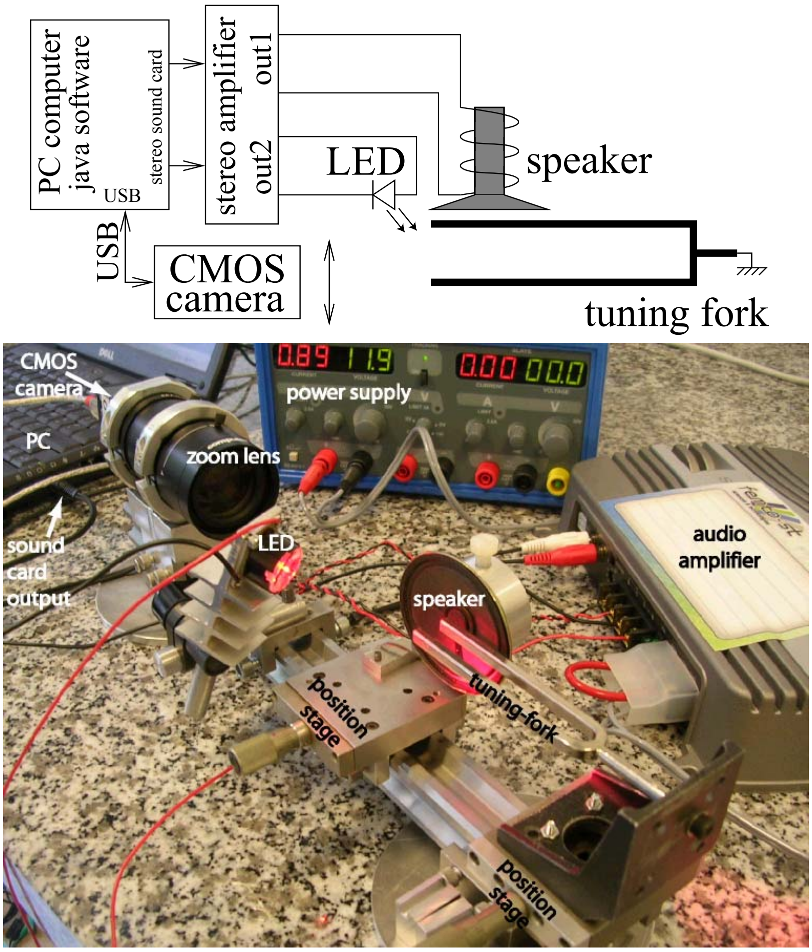

FIG. 1: Schematic and picture of the experimental setup.

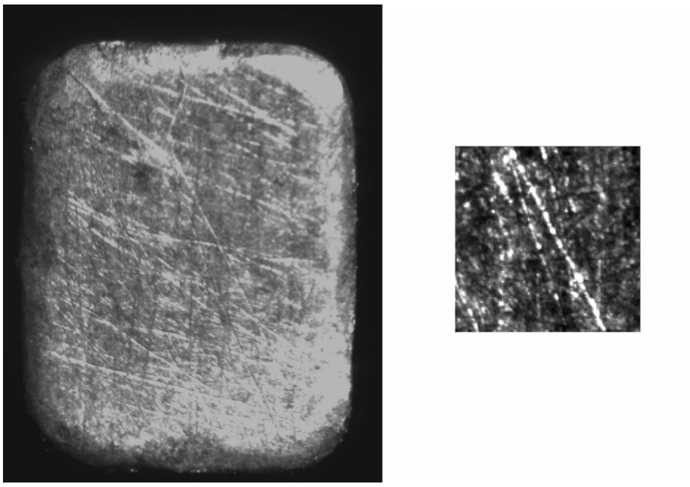

FIG. 2: Left: Image of the prong end face (5×4 mm^2) as recorded with the USB vision setup during oscillation. Right: 128×128 pixel image as acquired with a higher magnification for digital processing in order to extract the image displacement with respect to a reference image. (actual size: $742\times742\mu m^2$). Note that no specific pattern is visible: displacement retrieval is based on natural features such as surface roughness and defects.

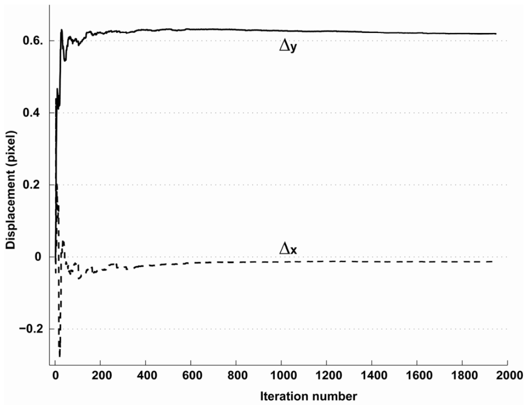

FIG. 3: Evolution of the estimated displacement value during the iterative process of the spectral phase algorithm.

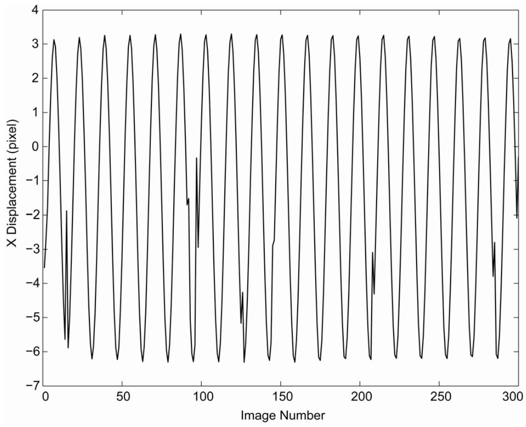

FIG. 4: Typical result of prong displacement measurement as reconstructed with the spectral phase algorithm during tuning vibration. The zero displacement position does not necessarily correspond to the central value since it is relative to the reference image.

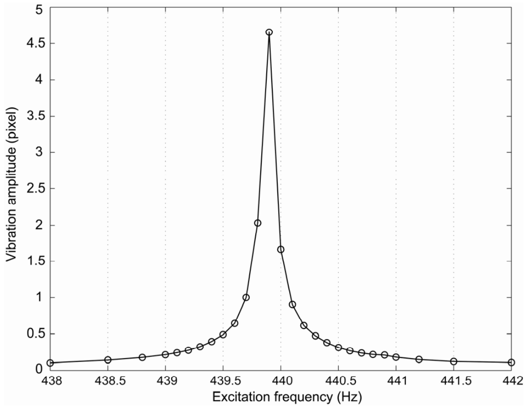

FIG. 5: Resonance curve of the tuning fork as reconstructed experimentally.

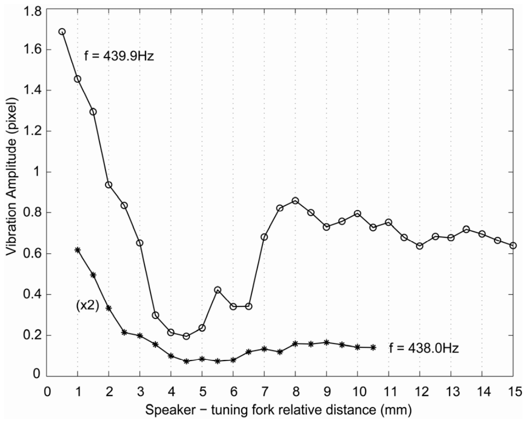

FIG. 6: Vibration amplitude versus relative distance between speaker and prong. Amplitude at 438Hz was amplified by two for better visibility.

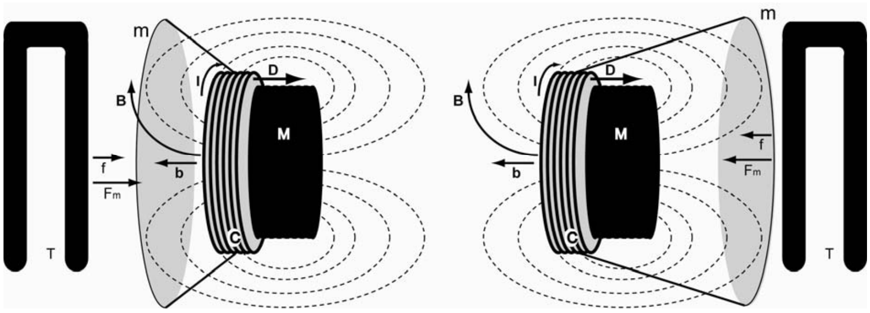

FIG. 7: Vectorial combination of the acoustic and magnetic forces produced by a speaker. m: membrane; M: permanent magnet; dashed lines: lines of the magnetic field; C: coil; T: tuning fork; **B**: induction due to M; **I**: current flowing through C; **D**: coil displacement resulting from I and B. **b**: induction due to C and **I**. **Fm**: permanent force exerted on the prong by the magnet; **f**: modulation of the magnetic force due to the coil. The acoustic force produced by the membrane motion is directed in the same direction than **D**. **b** and **f** change of direction with **I**. The magnetic and acoustic forces are in phase in the left case, while they are out of phase in the right case. The coil is placed on the side of the magnet in order to optimize the projection of the vectorial product of **B** and **I** in the displacement direction.

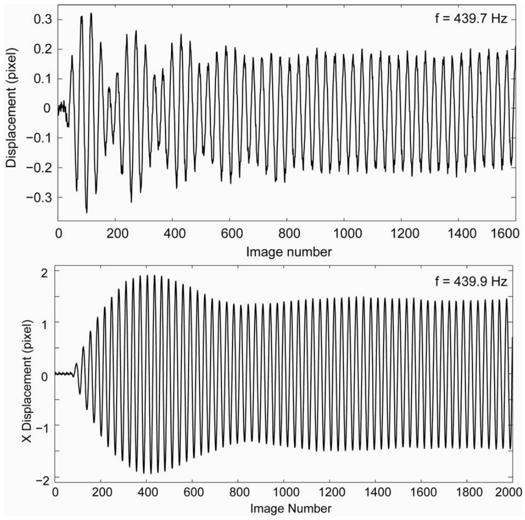

FIG. 8: Vibration amplitude versus time at start of excitation. The amplitude modulation is due to a beat between the forced frequency and the natural resonance frequency of the tuning fork. In this experiment the frequency shift between excitation and stroboscope was reduced to 1Hz for better visibility of the beat frequency.

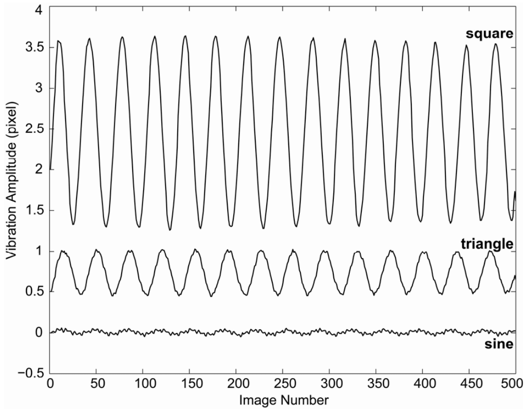

FIG. 9: Vibration amplitude with an excitation at 146.6Hz and for different signal shapes. Observations with a stroboscope frequency of 437.8Hz

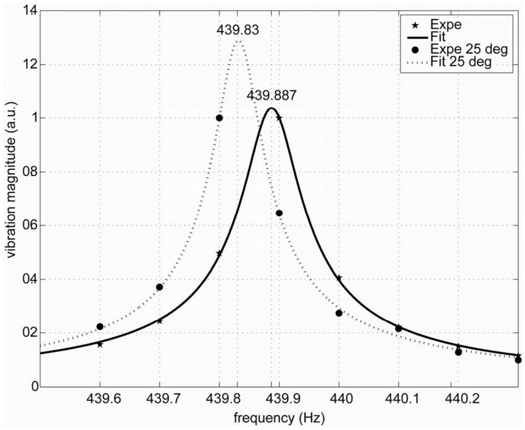

FIG. 10: Thermal drift of the resonance frequency as observed experimentally. The experimental data were fitted with a series resistance-inductance-capacitance equivalent circuit for accurate identification of the resonance frequency.

List of Tables

Frequency (Hz)	146.6	439.8	733	1026
sine shape (mV)	348	-	-	-
square shape (mV)	446	136	93	63
ratio f/f_0	-	3.3 (3)	4.8 (5)	7.08 (7)
triangle shape (mV)	281	31	12	8
ratio f/f_0	-	9.06 (9)	23.4 (25)	35 (49)
ratio $square/triangle$	1.58	4.4	7.7	7.9

TABLE I: Power spectral distribution for the different signal shapes as measured with a spectrum analyser. The f/f_0 ratio is compared to the expected value given between parentheses. Curves of Fig.9 have to be compared to the ratio of 4.4 at the resonant frequency.